



Electromechanical modeling of a motor–gearbox system for local gear tooth faults detection

Bilal El Yousfi ^{a,*}, Abdenour Soualhi ^a, Kamal Medjaher ^b, François Guillet ^a

^a Univ. Lyon, UJM de Saint Étienne, LASPI EA3059, 20 Avenue de Paris, 42334, Roanne Cedex, France

^b INPT-ENIT, LGP EA1905, 47 Avenue d'Azereix, 65000, Tarbes, France

ARTICLE INFO

Communicated by Y. Halevi

Keywords:

Electromechanical systems
Induction machine
Gearbox
Gear mesh stiffness
Modeling
Faults detection

ABSTRACT

Many of today's industrial applications are powered by electromechanical drives. Wind turbines, fuel based and hydroelectric generators or electric drivetrains are examples of these applications. Developing accurate models of these systems has attracted a significant interest in recent years, because it can help enormously to enhance their reliability and develop efficient maintenance strategies to avoid prominent failure modes. In this paper, motor–gearbox systems are investigated in their both mechanical and electrical aspects. An electrical model of an induction machine is coupled with a lumped parameter model of a two-stage gear system to build an integrated model of these systems. The coupling between these sub-models is realized in a way that allows to consider transient regimes. Furthermore, an improved potential energy method is used to determine the mesh stiffness of gear pairs considering actual gear shapes and an original method is proposed to refine stiffness curves based on the correlation measure with experimental measurements. The developed model is validated under varying operating conditions using vibration and electrical measurements and simulation results were in good agreement with experiment. Moreover, the model was investigated for the detection of gear tooth faults using both vibration and motor current signature analysis in time and frequency domains, the model response under faulty condition was satisfactory compared with the observed response.

1. Introduction

Electromechanical systems are one of the main components of nowadays industrial applications. From the energy production field, where almost all traditional and renewable energy production types are based on the conversion between electrical and mechanical power, to transport, industry and other application forms of these systems [1]. This is why understanding the interaction mechanism between mechanical and electrical parts of them can help greatly to improve their efficiency, reliability and practical useful life. As its name suggests, these systems mainly consist of two parts: electrical part, which is the motor or the generator depending on the application, and a mechanical part generally employed for alternating torque and speed values.

Thanks to their high productivity and energy cost ratio, induction machines are widely adopted in today's electromechanical applications [2]. They mainly consist of two parts, namely the stator, which is the fixed part of these machines and the rotor, which is the rotating part. When used as motoring device, the electric current in the rotor needed to produce torque is obtained via electromagnetic induction from the rotating magnetic field of the stator winding supplied by a three-phase supply system [3].

* Corresponding author.

E-mail address: bilal.elyousfi@univ-st-etienne.fr (B.E. Yousfi).

Almost, all electromechanical applications need a power transmission device to adjust torque and speed values. For this aim, gearboxes remain one of the most preferred options among all other solutions for industrials, because of their good efficiency and high precision [4]. Gearboxes are mainly composed of geared wheels of different diameters mounted on one or multiple stages.

Modeling motor-drive systems has attracted a significant attention in the last few decades [5]. Developing accurate models of these systems can help to understand their behavior; and therefore, diagnosing and prognosing failures to avoid misfunctions and catastrophic damages [6–10]. Existing models can be gathered into two main categories: models based on the torque oscillation theory (TOT) and models based on the lumped parameter theory (LPT). The next section emphasizes existing electromechanical models for local gear tooth faults detection and diagnostic based on both theories.

TOT-based models stand on understanding the mechanism of how stator current reflects characteristics of load torque. The different characteristic frequencies such as gear mesh, gear rotations and transmission errors are modeled as oscillations around the average load torque with subjectively chosen amplitudes based on experimental observations. In [11,12], a theoretical and an experimental investigation of a multi-stage transmission gearbox based on the TOT was performed to study the effect of gear teeth defects on the motor current signature. In [13,14], an experimental and analytical development based on the TOT was proposed to study the impact of mechanical faults in a single stage gear system on the current signal signature of a three-phase induction machine. In [15], TOT was used to analytically model planetary gearbox faults and air gap eccentricity under nonstationary conditions; then, the motor stator currents were analyzed for fault detection and diagnostic.

The second category is based on the use of the LPT method to model gearbox dynamics. Several models were proposed to estimate the effect of gear tooth faults on the system torsional vibration. In [16], an integrated electromechanical model of an asynchronous motor coupled with a simple stage gearbox was proposed to detect gear tooth faults based on simulated stator current analysis in stationary conditions. In [17], A dynamic mathematical model of an electric drive multistage gear system was developed to perform a modal analysis of the system and investigate the electromechanical interaction mechanism based on simulation. In [18], the authors studied the effect of internal excitations and unsymmetrical voltage sag on the dynamics of a motor–gear system using permeance network model of the induction motor coupled with a lateral torsional model of a planetary gear system. In [19], the authors proposed a simple gear model combined with a space-phase model of the induction motor to assess tooth faults in epicyclic gearboxes using the synchronous average of motor currents.

Generally, TOT-based models offer the advantage of simplicity, but they fail in quantifying the system excitations especially the fault oscillation components. Conversely, LPT-based models offer a good precision in terms of quantification of the different internal excitations but require deep knowledge in dynamic modeling and a set of parameters to be identified. Many works have been done in the modeling of motor–gearbox systems in the literature, but very few of them considered the validation of the simulation results with experimental measurements, especially those based on the LPT method. In this study, a double validation is performed for the developed model by the mechanical measurements (speed and acceleration) and the electrical measurements (phase currents).

Among the nonlinear parameters that need to be determined when modeling these systems with the LPT method, gear mesh stiffness constitutes the main source of excitation in geared systems. The main methods proposed in the literature to estimate the gear mesh stiffness (GMS) are the numerical method, the experimental method and the analytical method [20]. To this day, the numerical method seems to be the most accurate approach to estimate the GMS of gear pairs if it is conducted properly, but it is time-consuming and requires deep pre-knowledge in FE modeling. Analytical methods for GMS calculation are based on the potential energy method proposed in [21], they give satisfying results in very reduced time compared to FEM, but some phenomena such as teeth deformations were neglected in this method, which leads to miss-estimate some characteristics of the GMS such as the hand-over region between the single-tooth and the double-tooth mesh periods. Several attempts have been proposed over time to enhance the analytical method by considering complex phenomena such as the nonlinear Hertzian contact, teeth profile modifications and the gear body structure coupling effect [22–24]. An original method is proposed in this study to improve the GMS calculation using the analytical method proposed in [25] and the experimental vibration.

In this study, the motor–gearbox electromechanical model is emphasized on its both electrical and mechanical aspects. This is achieved by surveying both electrical and mechanical quantities simultaneously (currents and vibration) which enables to get more realistic results compared to real world measurements. The LPT is employed to derive the gearbox dynamic model. An original method is used to evaluate the GMS of gear pairs, this method is a compromise between the FEM and the analytical method, because it has the advantage of numerical methods to consider the real geometry of the gears for locating the contact points during the meshing process, and then it uses the analytical formula developed by the potential energy method to calculate the stiffness based on the gear real geometries, which leads to a big reduction in the computation time compared to the FEM. In addition, vibration measurement is used to improve the GMS curve in its transition phases. Then, this model is coupled with the dynamic model of the induction machine in a way that allows to consider transient operating conditions to build the final overall motor–gearbox model. The developed model is verified under varying operating conditions. Vibration and currents are analyzed for local tooth fault detection for both simulation and experiment.

This paper is organized as follows: Section 2 deals with the system modeling (induction machine model, gearbox dynamic model, gear mesh stiffness determination process and the final overall model). Section 3 presents a verification of model results under varying operating conditions with a dedicated experimental platform in healthy and faulty states. Finally, Section 4 concludes the paper and gives some perspectives.

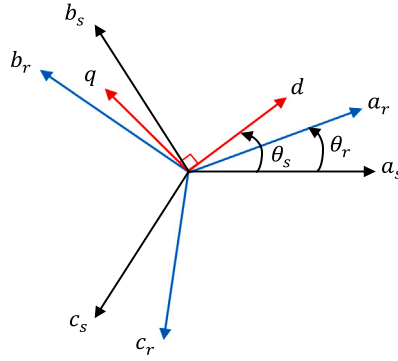


Fig. 1. Representation of phase coordinate and orthogonal dq frames.

2. System modeling

2.1. Electrical model

The models available to estimate the performance of an asynchronous motor are either numerical (FEM), analytical or by the magnetic equivalent circuits.

The FEM proposes to solve directly the basic physical equations of the motor using heavy numerical mathematical algorithms. From (i) the motor geometry, (ii) the characterization of the materials that compose it, (iii) by a discretization in small regions (mesh) and by using the boundary conditions of the problem, the software are able to predict the performance of the machine and in particular to offer detailed flux maps. They integrate magnetostatic and magnetodynamic modules and deal with even complex two-dimensional or three-dimensional geometry by the method of resolution of finite elements or differences [26].

The magnetic equivalent circuits model proposes to represent the operation of the induction motor by interconnected reluctances (or flux tubes). Kirchoff's laws are then used to solve the particular system to evaluate the fluxes in each of the reluctant elements. The resolution of the system is done numerically while the expression of the reluctances will be analytical and parameterized to the maximum. This method is based on dividing the structure of the machine into a number of elements which constitute what are called flow tubes or induction tubes [27].

The analytical approach enables to represent the behavior of the asynchronous machine by mathematical equations making it possible to study its behavior as a whole in a permanent or transient state. A reference dq_0 is defined by the choice of its rotation speed of reference. In our case, the dq_0 coordinate system rotates synchronously with the rotating magnetic field to study the motor's response to weak disturbances around a given speed. This modeling makes it possible to obtain a very correct overall approach to the performance of the machine (by global considerations on flux, torques, etc.).

Although the modeling of the magnetic equivalent circuits seems suitable for the detection of local defects of the gear teeth, its sensitivity can be reduced for small defects because of the undulations caused by the passage of the stator and rotor notches of the asynchronous machine, even by eliminating the power supply frequency of the signal. It is therefore preferable to favor the analytical model for the reasons mentioned previously. In addition, it should be noted that the implementation of the modeling of the magnetic equivalent circuits requires a very good knowledge of the phenomena inherent in the machine. In case of doubt, it is often preferable to first use methods such as FEM to correctly understand the trajectory of the flux. The main difficulty with this type of modeling obviously lies in identifying the different induction tubes.

A schematic representation of a three-phase induction machine in the analytical approach is given in Fig. 1, where $a_{s,r}$, $b_{s,r}$, $c_{s,r}$ are stator and rotor phases. Both of stator and rotor carries three phase windings placed in an $2\pi/3$ electrical angle. Each winding is modeled with a couple of resistance $R_{s,r}$ and inductance $L_{s,r}$.

Mathematical modeling of the induction motor by the analytical method stands on the definition of magnetic fluxes ϕ_i and phase currents i_i based on the Maxwell–Faraday equations of electromagnetic induction [28]. The Park's theory is employed to transform the model equations from the phase coordinate frame to an orthogonal (dq) frame using Park's transformation matrix P (Fig. 1). This transformation enables to reduce the system dimension and get constant coefficients in the differential equations system which leads to a significant simplification of the calculation process.

$$[P] = \sqrt{\frac{2}{3}} \begin{bmatrix} \cos(\psi) & \cos(\psi - \frac{2\pi}{3}) & \cos(\psi + \frac{2\pi}{3}) \\ -\sin(\psi) & -\sin(\psi - \frac{2\pi}{3}) & -\sin(\psi + \frac{2\pi}{3}) \\ \frac{1}{\sqrt{2}} & \frac{1}{\sqrt{2}} & \frac{1}{\sqrt{2}} \end{bmatrix} \quad (1)$$

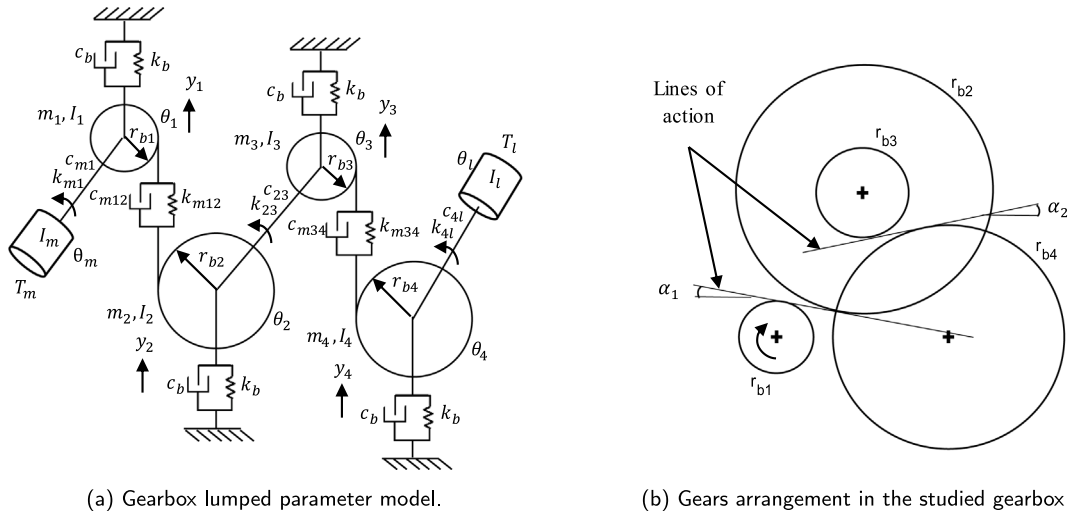


Fig. 2. Gearbox lumped parameter model.

Explicit development of the electrical equations of the induction machine can be found in [5]. The final adopted electric equations in the dq frame are expressed as follows:

$$\begin{cases} \frac{d}{dt} i_{ds} = \frac{1}{\sigma L_s} v_{ds} - \left(\frac{1}{\sigma T_s} + \frac{1}{T_r} \frac{1-\sigma}{\sigma} \right) i_{ds} + \omega_s i_{qs} + \frac{1}{T_r L_m} \frac{1-\sigma}{\sigma} \phi_{dr} + \frac{1}{L_m} \frac{1-\sigma}{\sigma} \omega_m \phi_{qr} \\ \frac{d}{dt} i_{qs} = \frac{1}{\sigma L_s} v_{qs} - \left(\frac{1}{\sigma T_s} + \frac{1}{T_r} \frac{1-\sigma}{\sigma} \right) i_{qs} - \omega_s i_{ds} + \frac{1}{T_r L_m} \frac{1-\sigma}{\sigma} \phi_{qr} - \frac{1}{L_m} \frac{1-\sigma}{\sigma} \omega_m \phi_{dr} \\ \frac{d}{dt} \phi_{dr} = \frac{L_m}{T_r} i_{ds} - \frac{1}{T_r} \phi_{dr} + (\omega_s - \omega_m) \phi_{qr} \\ \frac{d}{dt} \phi_{qr} = \frac{L_m}{T_r} i_{qs} + \frac{1}{T_r} \phi_{qr} - (\omega_s - \omega_m) \phi_{dr} \end{cases} \quad (2)$$

where: $\sigma = 1 - L_m^2 / L_r L_s$, $T_r = L_r / R_r$, $T_s = L_s / R_s$ and ω_s, ω_m are the synchronous and mechanical speeds, v_{ds}, v_{qs} are the supply voltages and L_m is the magnetizing inductance.

The electromagnetic torque expression is derived from the conservation of the instantaneous power as follows:

$$T_{em} = \frac{p L_m}{L_r} (\phi_{dr} i_{qs} - \phi_{qr} i_{ds}) \quad (3)$$

Finally, we subtract the torque loss due to friction f to get the final expression of motor torque:

$$T_m = T_{em} - f \omega_m \quad (4)$$

2.2. Mechanical model

The lumped parameter theory is used to model the two-stage spur gear system as represented in Fig. 2(a). In this approach, gears are modeled with concentrated masses and inertias (m_i, I_i), coupling elements (shafts) between elements i and j are represented with spring-damper systems of parameters (k_{ij}, c_{ij}). Only radial deformations of bearings are considered with constant stiffness and damping coefficients (k_b, c_b). The meshing rigidity variation is modeled with a spring-damper system (k_{mij}, c_{mij}), where the calculation process of the meshing stiffness k_{mij} between pinion i and gear j is detailed in Section 2.3. y_i is the linear displacement in the line of action direction (see Fig. 2(b)) and θ_i is the angular displacement. Subscripts 1, 2, 3, 4, m and l refer to the four gears, motor and load respectively. Some phenomena such as backlash and gears friction were neglected in this model.

The system model is derived using Lagrange's equations of motion as follows:

$$\frac{d}{dt} \frac{\partial L}{\partial \dot{q}_i} - \frac{\partial L}{\partial q_i} - \frac{\partial D}{\partial \dot{q}_i} = F_{ext} \quad (5)$$

where: $L = T - V$ is the system's Lagrangian, T, V and D are the system's kinetic, potential and Rayleigh's dissipation energies respectively, F_{ext} is the vector of external forces and q_i is the vector of system's variables. Applying Eq. (5) with respect of all

system variables leads to the following system of equations:

$$\begin{cases} m_1 \ddot{y}_1 = -k_b y_1 - c_b \dot{y}_1 + F_{k12} + F_{c12} \\ m_2 \ddot{y}_2 = -k_b y_2 - c_b \dot{y}_2 - F_{k12} - F_{c12} \\ m_3 \ddot{y}_3 = -k_b y_3 - c_b \dot{y}_3 + F_{k34} + F_{c34} \\ m_4 \ddot{y}_4 = -k_b y_4 - c_b \dot{y}_4 - F_{k34} - F_{c34} \\ I_1 \ddot{\theta}_1 = k_{m1} \Delta \theta_{m1} + c_{m1} \Delta \dot{\theta}_{m1} - r_{b1} (F_{k12} + F_{c12}) \\ I_2 \ddot{\theta}_2 = -k_{23} \Delta \theta_{23} - c_{23} \Delta \dot{\theta}_{23} + r_{b2} (F_{k12} + F_{c12}) \\ I_3 \ddot{\theta}_3 = k_{23} \Delta \theta_{23} + c_{23} \Delta \dot{\theta}_{23} - r_{b3} (F_{k34} + F_{c34}) \\ I_4 \ddot{\theta}_4 = -k_{4l} \Delta \theta_{4l} - c_{4l} \Delta \dot{\theta}_{4l} + r_{b4} (F_{k34} + F_{c34}) \\ I_m \ddot{\theta}_m = T_m - k_{m1} \Delta \theta_{m1} - c_{m1} \Delta \dot{\theta}_{m1} \\ I_l \ddot{\theta}_l = -T_l + k_{4l} \Delta \theta_{4l} + c_{4l} \Delta \dot{\theta}_{4l} \end{cases} \quad (6)$$

where: $\Delta \theta_{ij} = (\theta_i - \theta_j)$ and $\Delta \dot{\theta}_{ij} = (\dot{\theta}_i - \dot{\theta}_j)$. The elastic and damping mesh forces F_{kij}, F_{cij} , are expressed as follows:

$$\begin{cases} F_{kij} = k_{mij} (r_{bi} \theta_i - r_{bj} \theta_j - y_i + y_j) \\ F_{cij} = c_{mij} (r_{bi} \dot{\theta}_i - r_{bj} \dot{\theta}_j - \dot{y}_i + \dot{y}_j) \end{cases} \quad (7)$$

The shaft torsional stiffness between elements i and j is determined theoretically as follows:

$$k_{ij} = G \frac{\pi (d_{ou}^4 - d_{in}^4)}{32l} \quad (8)$$

where G is the shear modulus, d_{in}, d_{ou} , are inner and outer shaft diameters and l is its length. The damping coefficients for coupling shafts and gear meshing are determined considering the following expressions:

$$c_{ij} = 2\xi_s \sqrt{k_{ij} \left(\frac{1}{I_i} + \frac{1}{I_j} \right)^{-1}}, \quad c_{mij} = 2\xi_m \sqrt{\bar{k}_{mij} \left(\frac{r_{bi}^2}{I_i} + \frac{r_{bj}^2}{I_j} \right)^{-1}} \quad (9)$$

where $\xi_s = 0.005$ and $\xi_m = 0.1$ are damping ratios of shafts and gear meshing respectively [29].

2.3. Gear mesh stiffness calculation

In this paper, the analytical method proposed in [25] is adopted for the evaluation of the gear mesh stiffness of the two gear pairs. In this method, the mesh stiffness calculation process was discretized for local gear tooth faults consideration and a contact detection algorithm was proposed to determine the contact points at each meshing step. A brief description of this method is done in Algorithm 1 [30].

This method is improved in this work by considering the real geometries of the test bench gear pairs (see Fig. 4). The 3D models of the different gears were downloaded and verified from the manufacturer website using the references indicated in the gears. Then, the gear geometries were extracted using a dedicated computer-aided design software. This allowed considering actual gear geometry with all modifications done to the gear tooth shape such as root curve form, addendum correction factor, tooth tip corner, and tooth width variation along the tooth length direction as shown in Fig. 4. In addition, the gear body component of the mesh stiffness is evaluated considering the actual foundation form of each gear.

Algorithm 1 GMS calculation process in the proposed method.

1. Tooth profile extraction.

Use a CAD software to extract the tooth profile, apply the desired resampling and save its coordinates in a vector T_p .

2. Gears' matrixes reconstruction.

Use the extracted gear tooth profile to build the pinion and gear 2D matrixes P and G respectively as follows:

for $z=1$ to Z do

$$T_{p,z} = T_p(\theta = z \times \frac{2\pi}{Z})$$

{rotate the tooth profile with the angle θ }

$$M(i, z) = T_{p,z}$$

end for

where M is the gear matrix and Z is the number of teeth.

3. Pinion and gear angular position updating.

$$P \leftarrow P(\theta_p^t) \quad G \leftarrow G(\theta_g^t)$$

{rotate the pinion and gear matrixes}

4. Contact points detection.

Use the distance minimization to get the contact points between the pinion and gear points at this iteration.

5. Stiffness calculation

Use the contact points to evaluate the teeth elementary stiffnesses by Eqs. (10) to (14). Then, use Eq. (15) to determine the total stiffness at this iteration.

6. Return to 3.

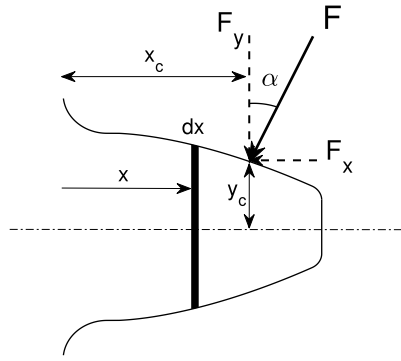


Fig. 3. Gear tooth representation in the potential energy method.

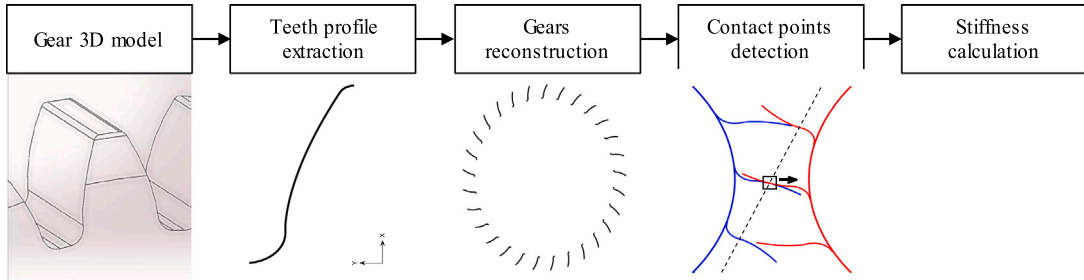


Fig. 4. Gear mesh stiffness evaluation process.

In this algorithm of GMS determination, gear faults are modeled directly with their geometries as in the FEM by modifying the corresponding gear matrix. This allows to consider variable-shaped defects as was proved in [25] for non-uniform spalls and pits. As an example, if the z th tooth is broken, it is modeled by setting the tooth corresponding column $T_{p,z}$ in the gear matrix to zero.

In the potential energy method, the gear tooth is modeled as a nonuniform cantilever beam as shown in Fig. 3, and the stiffness components are derived from the different energies stored in the gear tooth body when subjected to the contact force F . The gear mesh stiffness components considered are: Hertzian component k_h , bending component k_b , axial-compression component k_a , shearing component k_s and fillet foundation component k_f .

$$k_h = \frac{\pi E L_x}{4(1-\nu^2)} \quad (10)$$

$$\frac{1}{k_a} = \int_0^{x_c} \frac{\sin^2 \alpha}{E S_x} dx \quad (11)$$

$$\frac{1}{k_b} = \int_0^{x_c} \frac{(x_c \cos \alpha - y_c \sin \alpha)^2}{E I_x} dx \quad (12)$$

$$\frac{1}{k_s} = \int_0^{x_c} \frac{1.2 \cos^2 \alpha}{G S_x} dx \quad (13)$$

$$\frac{1}{k_f} = \frac{\cos^2 \alpha}{L_{fo} E} \left\{ L^* \left(\frac{u_f}{S_f} \right)^2 + M^* \left(\frac{u_f}{S_f} \right) + P^* (1 + Q^* \tan^2 \alpha) \right\} \quad (14)$$

where E is Young modulus, ν is Poisson's ratio, G is shear modulus, L_x , S_x and I_x are the tooth width, the tooth cross section area and moment of inertia respectively at coordinate x along the tooth length direction. x_c , y_c and α are represented in Fig. 3. L_{fo} is the gear foundation width and parameters u_f , S_f , L^* , M^* , P^* , Q^* are detailed in [31]. Once all components of gear mesh stiffness

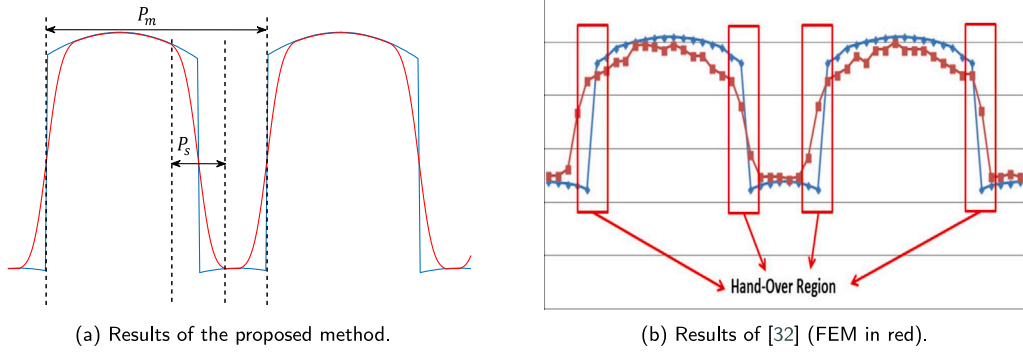


Fig. 5. Smoothing of the transition phases.

are calculated, the total stiffness of mating gears k_m can be determined with the following formulas:

$$k_m = \sum_{i=1}^{N_c} \frac{1}{\frac{1}{k_n} + \sum_j \left(\frac{1}{k_{f,i,j}} + \frac{1}{k_{a,i,j}} + \frac{1}{k_{b,i,j}} + \frac{1}{k_{s,i,j}} \right)} \quad (15)$$

2.3.1. Gear mesh stiffness smoothing

We know from the FEM results that the hand-over region between the single-tooth and the double-tooth mesh regions is smoother than it is found by analytical methods [32,33]. The idea here was to use one of the measured quantities that is directly impacted by this transition region to correct the GMS curve in these hand-over regions, and we observed that the acceleration signal is highly sensitive to this transition form. Using the dynamic response from test structures to correct model parameters is a well known procedure called *model updating* [34]. We first used a simple moving average filter to smooth this hand-over region but the start-up and the ending sharp edges induced undesired outliers on the acceleration signal and comparing with the FEM results we found that the Gaussian-weighted moving average (GWMA) filter was more convenient because of its capability to minimize start-up and ending transient edges as illustrated in Fig. 5. Physically, this effect could be explained by the gradual engagement and disengagement of gear teeth during meshing process, because when the driving gear get in contact with the driven gear, there is a small interval of pre-deformation of the two gears before the driven gear is trained; in this interval, the stiffness value grows gradually. The same phenomenon is applied in the disengagement phase.

The smoothing rate $\tau_s = P_s / P_m$ is fixed based on the similarity measure with the experimental acceleration using the correlation coefficient. A normalization operation is necessary because we know that there is always a shift between the simulated and the experimental operating frequencies, and the acceleration amplitude is partially attenuated by the bearing housing. Also, the cross correlation factor is used to eliminate the phase shift between these two signals. The aim here is to compare the form of the acceleration signal because we observed that this transition region has a direct impact on the acceleration impulses.

As showed in Fig. 5, the smoothing results in our study are highly correlated with those obtained using the FEM by authors in [33]. These results are also compatible with those of FEM found in [35,36]. It should be mentioned here that one must refine the calculation in this hand-over region in order to get accurate results by the FEM. In addition, the aim of this method was mainly to offer a low cost, time-efficient and easy-implemented method for estimating this transition curve, because FEM gives excellent results but it is time-consuming, needs specific materials and tools, and a deep pre-knowledge in FE modeling.

2.4. Overall electromechanical model

The overall model of the studied motor-gearbox system is represented in Fig. 6. Inputs of this model are the three-phase supply voltages (v_{as}, v_{bs}, v_{cs}) and the load torque T_l . The model consists of two main parts: the electrical model of the induction machine and the mechanical model of the gearbox. These two sub models interact with each other at each time step through motor torque T_m and rotational speed $\omega_m = \dot{\theta}_m$. Outputs of the model are the three-phase currents (i_{as}, i_{bs}, i_{cs}) and the gearbox vibration \ddot{y}_i of the four gears.

As illustrated in the mechanical sub model of Fig. 6, the feeding in mesh stiffness is done with respect to the actual gear angular positions, which allows considering the speed fluctuations during the simulation process.

3. Results and discussion

3.1. Experimental set-up

The proposed theoretical model is experimentally validated using the electromechanical drivetrain of Fig. 7. This testing set-up consists of a 2.2 kW, 50 Hz, 400 V star-connected, 2-pole, 2905 rpm three-phase induction motor, driven with a variable frequency

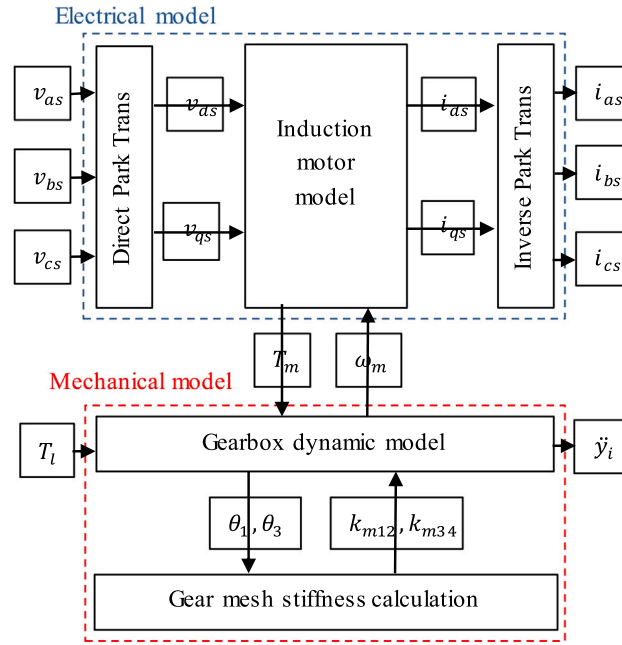


Fig. 6. Overall model of the motor-gearbox system.

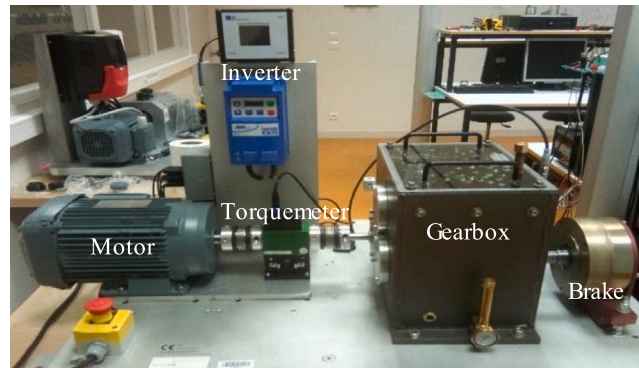


Fig. 7. Test bench for model validation.

inverter. A two-stage parallel-shaft gearbox made up of a 29–100 tooth gear pair in the input stage and a 36–90 tooth gear pair in the output stage. the test bed is loaded with a constant torque magnetic particle brake controlled by a constant voltage DC power supply. A torque meter sensor is placed between motor and gearbox to estimate torque and speed developed by motor. An accelerometer is placed in the horizontal direction of the second stage pinion. Supplied phase voltages and currents are acquired at the inverter output. Acquisition time is $T = 10$ s with a sampling frequency $F_s = 25.6$ kHz for the acceleration and electrical signals and $F_s = 10$ Hz for the speed and torque measured with the torque meter.

3.2. Simulation results

The electrical and mechanical parameters used for model simulation are listed in Table 1.

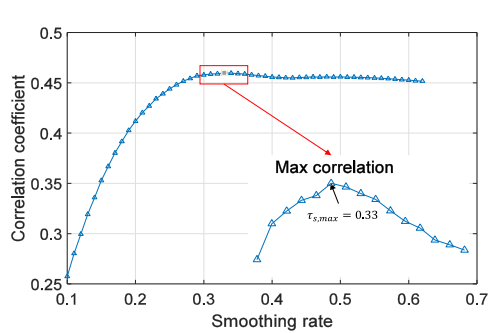
3.2.1. Gear mesh stiffness results

The evolution of the correlation coefficient as a function of the smoothing rate is represented in Fig. 8(a). Its value grows rapidly to reach a maximum correlation factor at a smoothing rate $\tau_s = 0.33$; then, it falls slowly for greater rate values. Fig. 8(b) illustrates the final mesh stiffness curves for the two gear pairs before and after the smoothing operation. The same smoothing rate was applied to the two gear pairs. Fig. 8(c) shows the resulting simulated acceleration signal at maximum correlation value superposed with the measured one. One can see that the result of the acceleration signal is very similar to the measured acceleration; we will see later that even spectrums become highly correlated after this smoothing operation.

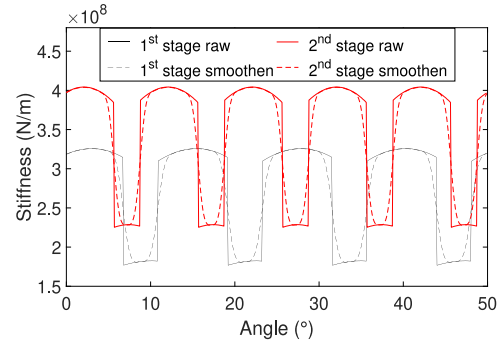
Table 1
Simulation parameters.

Symbol	Quantity	Value	Symbol	Quantity	Value
E	Young modulus	2.068×10^{11} Pa	I_3	Second pinion inertia	1.21×10^{-4} kg m ²
ν	Poisson's ratio	0.3	I_4	Second gear inertia	3.89×10^{-3} kg m ²
m	Module	1.5 mm	I_m	Motor inertia	6.63×10^{-3} kg m ²
k_b	Bearing stiffness	6.56×10^8 N/m	I_l	Load inertia	3.3×10^{-4} kg m ²
c_b	Bearing damping	1.8×10^3 N s/m	R_s^a	Stator resistance	3.45 Ω
m_1	First pinion mass	0.16 kg	R_r^a	Rotor resistance	1.66 Ω
m_2	First gear mass	1.74 kg	L_s^a	Stator inductance	0.419 H
m_3	Second pinion mass	0.294 kg	L_r^a	Rotor inductance	0.419 Ω
m_4	Second gear mass	1.79 kg	L_m^a	Magnetizing inductance	0.4 H
I_1	First pinion inertia	4.76×10^{-5} kg m ²	P	Pole pairs	1
I_2	First gear inertia	4.82×10^{-3} kg m ²	f	Motor friction coefficient	0.0016

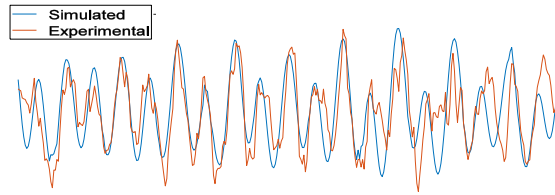
^aThese parameters were delivered by the manufacturer.



(a) Correlation factor as a function of the smoothing rate.



(b) Gear mesh stiffness of the two gear pairs.



(c) Simulated and experimental vibration superposed.

Fig. 8. Gear mesh stiffness smoothing results.

3.2.2. Model validation under healthy conditions

First, the developed model is verified under healthy conditions at different speeds and load levels (LL's). 12 scenarios were adopted to test the model accuracy under varying operating conditions by combining three supply frequencies (25 Hz, 35 Hz, 45 Hz) with four LL's (0%, 25%, 50%, 75%).

The measured input phase supply voltage at 25 Hz and 50% LL is represented in Fig. 9. A pass band filter was applied to these voltages to extract the amplitude of the nominal signal of them for model simulation. Using the raw measured voltages leads to the fluctuations of the system response around its nominal value, since the aim in this part is to compare the nominal values of simulated response with the measurements, we did not consider these fluctuations for model simulation. In addition, the aim behind modeling is to be able to predict the system response for unmeasured situations where supply voltages would be represented with perfect sine waves of amplitudes proportionals to the desired supply frequency.

Fig. 10 shows the gear mesh stiffness evolution of the first and second stages in the initial transient phase. As mentioned in Section 2.4, the mesh stiffness value at each time step is determined based on the current gears' angular position; this allows us to consider the transient phases during the simulation.

Fig. 11 shows the simulated dq frame currents issued by the developed model and those estimated by Park transformation of the filtered measured three-phase currents. One can see that model results are in good agreement with the measured ones.

Fig. 12 shows the measured and simulated acceleration signals taken at the pinion of the gearbox second stage on the horizontal direction. The difference in acceleration magnitudes is mainly due to the model parameter uncertainties and the attenuation caused by the gearbox housing and the sensor support.

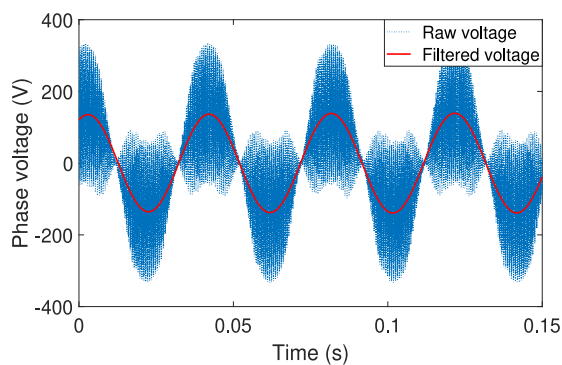


Fig. 9. Phase supply voltage at 25 Hz.

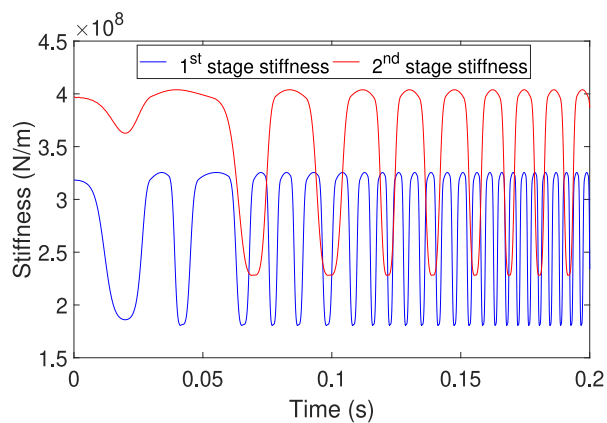


Fig. 10. Gear mesh stiffness evolution during simulation.

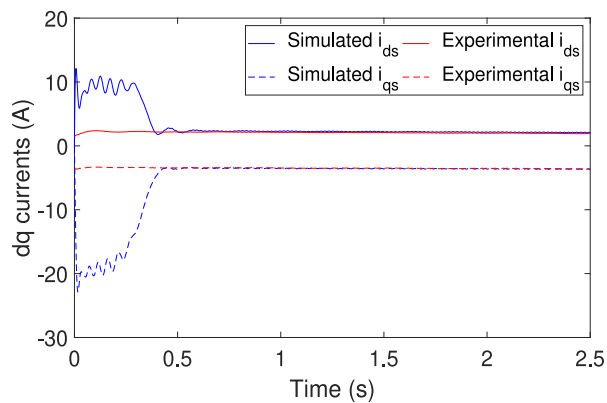


Fig. 11. Simulated vs. experimental dq currents.

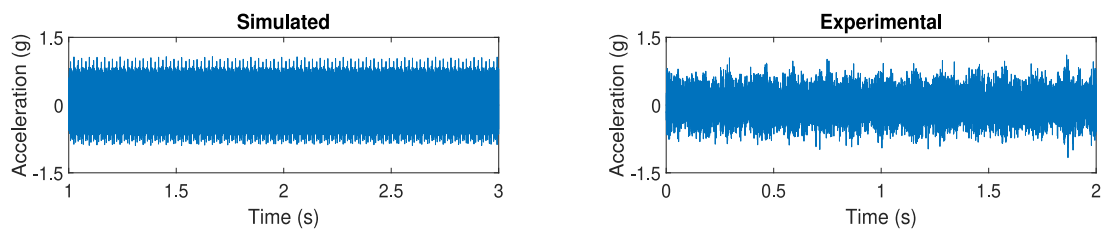


Fig. 12. Experimental vs. simulated vibration signal.

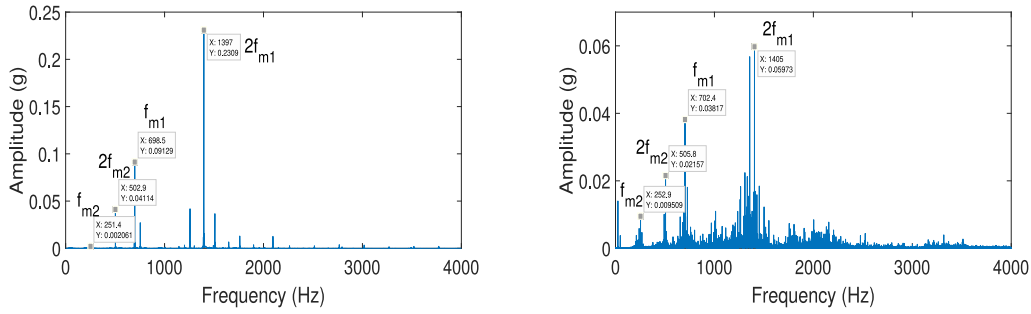


Fig. 13. Experimental vs. simulated vibration spectrums.

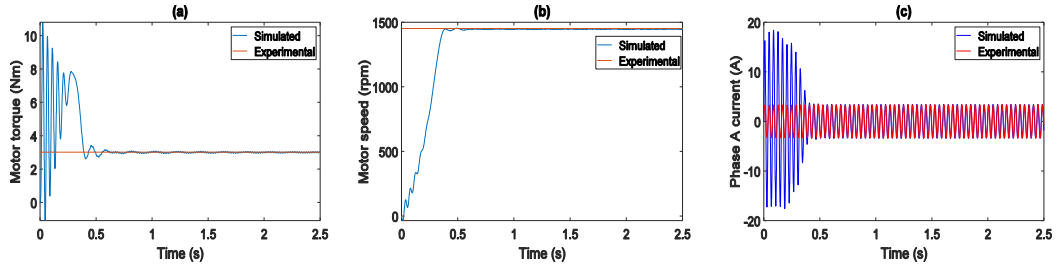


Fig. 14. Experimental vs. simulated: motor torque (a), motor speed (b) and the first phase current (c).

Table 2

Motor speed and current RMS at varying load levels (LL's) and supply frequencies.

F_s (Hz)	LL (%)	Supply voltage amplitude (V)	Motor speed (rpm)			Phase current RMS (A)		
			Sim	Exp	ϵ (%)	Sim	Exp	ϵ (%)
25	0	140.26	1489.8	1485.8	0.27	1.505	1.442	4.19
	25	138.79	1473.0	1473.2	0.00	1.744	1.650	5.39
	50	138.67	1446.0	1450.0	0.28	2.380	2.370	0.42
	75	138.83	1418.0	1428.0	0.7	3.15	3.13	0.63
35	0	196.74	2089.7	2086.0	0.18	1.520	1.450	4.61
	25	194.78	2076.4	2074.4	0.10	1.690	1.650	2.37
	50	194.15	2052.0	2054.0	0.10	2.275	2.265	0.44
	75	194.20	2024.0	2430.0	0.3	3.076	3.070	0.20
45	0	254.32	2689.0	2684.0	0.19	1.535	1.520	0.98
	25	251.76	2674.4	2671.52	0.11	1.753	1.753	0.00
	50	250.67	2653.0	2653.1	0.00	2.278	2.291	0.57
	75	249.95	2629.0	2631.2	0.10	3.036	3.040	0.13

In Fig. 13 are represented spectrums of simulated and measured vibrations. We can see that the two spectrums are highly correlated; the spectrum of measured vibration contains more noise and sidebands due to misalignments, runout errors and mounting errors in the real system.

Fig. 14 represents the measured and simulated motor torque, motor speed and the stator first phase current, the measured motor speed and torque are represented with their mean values, because the torquemeter used in the test bench does not allow to have the precise fluctuations of them. We can see that, globally, the simulation results are similar to the measured ones. The simulated steady state torque and motor speeds are not perfectly constant because of the fluctuations of supplied voltages; this makes the model more realistic when compared to experimental measurements. A small shift between the experimental and the simulated results exists mainly due to uncertainties in model parameters.

Experimental and simulated steady state motor speed and phase-current RMS value at different supplied frequencies and load levels (LL's) are listed in Table 2. Globally, the input voltage amplitude is proportional to the operating frequency, regardless of the applied load level, but a tiny difference is observed between the unloaded and the loaded cases that could be related to the inverter functioning mechanism. The experimental observations and the simulation results of the speed and phase current are in good agreement. When the system is charged with high loads, the speed decreases and the phase current increases to develop sufficient torque. The gap between the experimental and the simulated values varies with frequency and load level variation.

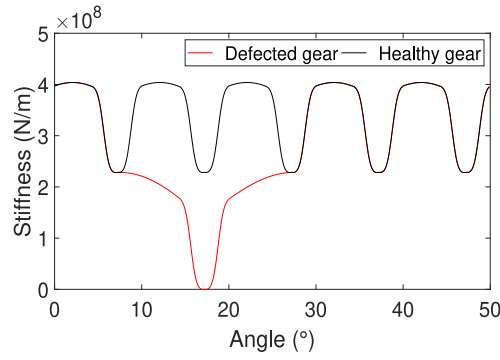


Fig. 15. Gear mesh stiffness of defective gear.

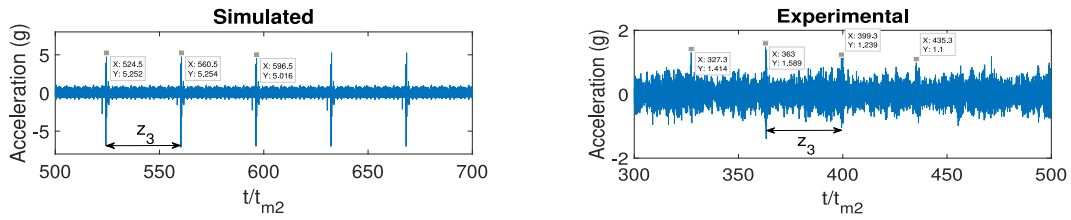


Fig. 16. Experimental vs. simulated vibration with a broken tooth.

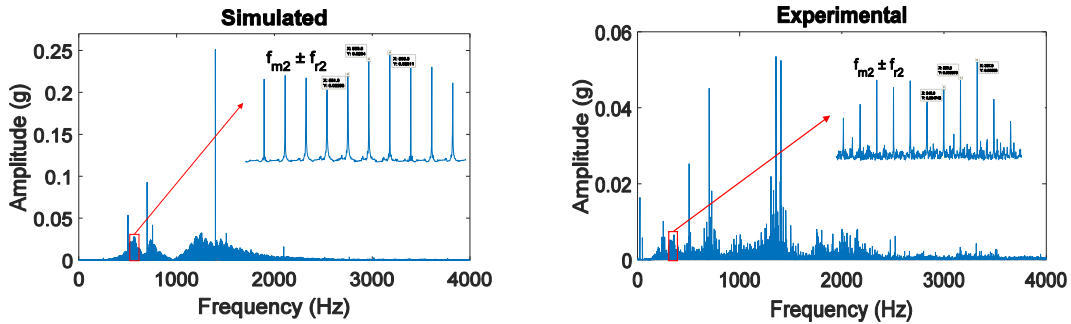


Fig. 17. Experimental vs. simulated vibration spectrum of broken tooth.

3.2.3. Model validation under faulty conditions

In Fig. 15 is represented the gear mesh stiffness curve of the second stage gear pair considering the gear tooth fault. A completely broken tooth fault was modeled in the second stage pinion and the corresponding stiffness was calculated as described in Section 2.3. The fault presence causes a local reduction in the mesh stiffness curve because of the contact loss at the fault position.

As shown in Fig. 16, a local gear tooth defect causes a local amplification of the acceleration signal because of the reduction of gear teeth resistance at these defected zones. The distance separating defect peaks corresponds to the teeth number of the faulty gear $Z_3 = 36$ since the time axis is normalized with the second gear mesh period t_{m2} .

In the frequency domain, a local gear tooth defect causes the apparition of a band of peaks separated with the rotation frequency of the defected gear $f_{r2} = 7$ Hz as illustrated in Fig. 17. The defect peaks magnitude in the simulated signal was close to those of experimental signals, which support the effectiveness of the smoothing operation of the gear mesh stiffness done in this study.

Fig. 18 represents the simulated phase current spectrum for healthy and faulty states at (25 Hz, 75% LL), the gear mesh frequencies were modulated by the electrical supply frequency: $|f_{mi} \pm f_s|$. The presence of tooth defect causes the raise of two overlapped sidebands distant with the defected pinion rotation frequency $f_{r2} = 7$ Hz.

Analyzing the measured phase current signals for the detection of the pinion fault was challenging for many reasons. First, the defect is located at the furthest stage from the motor, which results in a strong attenuation of fault components. Another factor is the high noise in the electrical signals, the supply voltage noise of Fig. 9 will also be reflected to the current signal, which makes the detection operation more complicated. To overcome these issues, the measured current signal is first de-noised in this study using the empirical mode decomposition principle by deriving the average curve of the lower and upper envelopes of the current

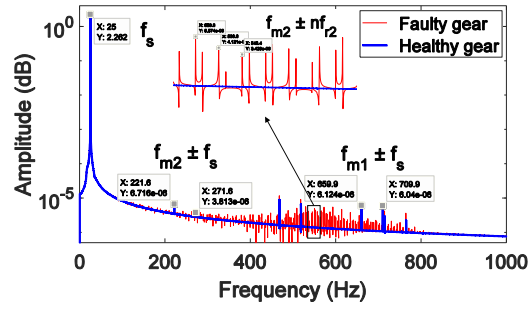


Fig. 18. Simulated current spectrums for healthy and faulty cases.

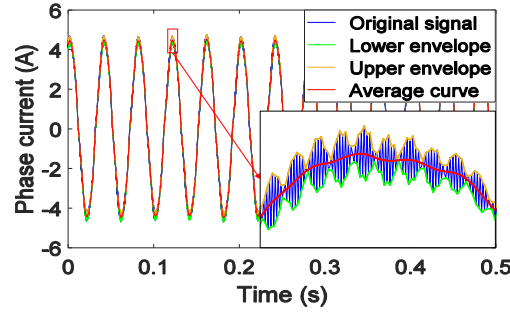
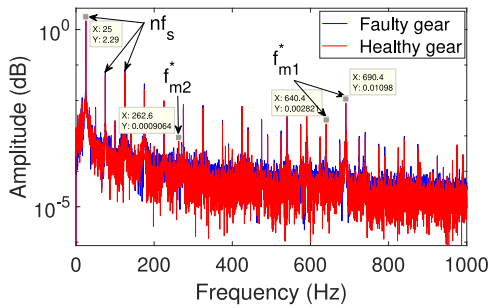
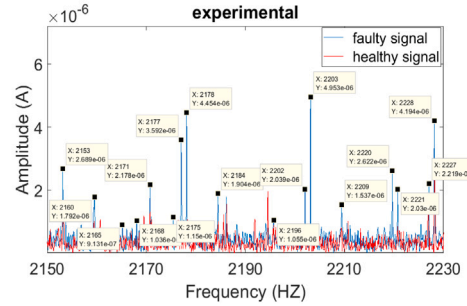


Fig. 19. Phase current de-noising.



(a) Current spectrums of healthy and faulty signals



(b) Fault manifestation on the current spectrum.

Fig. 20. Experimental phase current spectrum.

signal as illustrated in Fig. 19. This decomposition helps to eliminate the undesired electrical noise while preserving the main curve fluctuations of the nominal current curve.

An efficient way to distinguish mechanical components from electrical ones is to superpose multiple spectrums with a tiny lag in the LL's. This lag will cause a small difference in speed which will create a constant shift between mechanical peaks in the spectrum whereas electrical peaks remain unchanged. We observed that the lag created in electrical spectrum is equal of that of vibration one. Comparing the values of these lags with vibration spectrum will help us to isolate the different mechanical phenomena in the current spectrum. As illustrated in Fig. 20(a), gear mesh frequencies of the two stages were identified at $f_{m1}^* = f_{m1} \pm n f_s + f_r$ and $f_{m2}^* = f_{m2} \pm n_s f_s \pm n_2 f_{r2} \pm n_1 f_{r1} + f_r$ (n_i are integers).

As illustrated in Fig. 20(b), two overlapped bands of peaks distant by the defected pinion rotation frequency f_{r2} with the same overlapping-lag as in simulation results were observed in experimental spectrums of the faulty signal. This overlapping effect is caused by the modulation with supply frequency f_s .

Current analysis results have shown that both simulation and experiment contain mechanical excitation components. The difference is that in experimental signal, these excitations are modulated by the gears rotation frequencies in addition to the electrical supply frequency. As mentioned earlier, this is mainly due to model parameters uncertainties, mounting errors and runout errors in the real system.

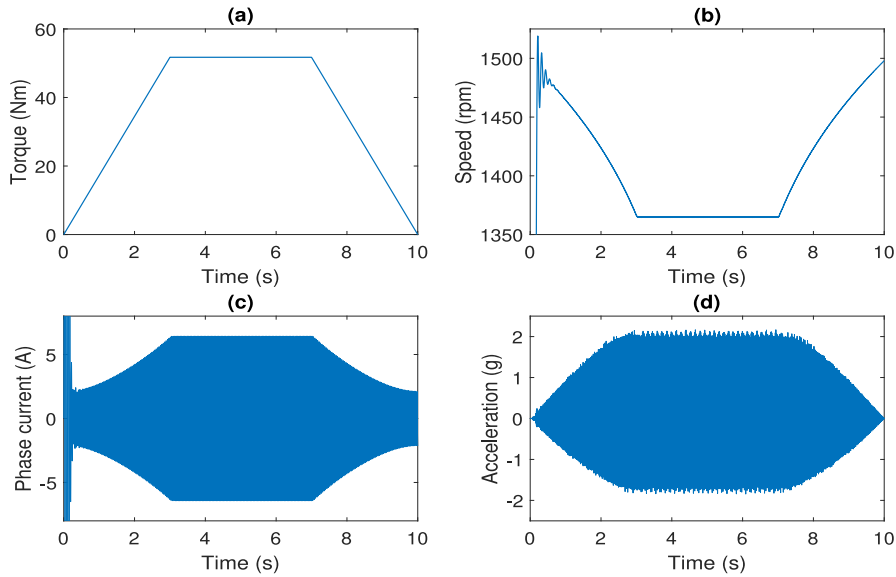


Fig. 21. Model response for a varying load: (a) applied torque; (b) motor speed; (c) phase current; (d) acceleration.

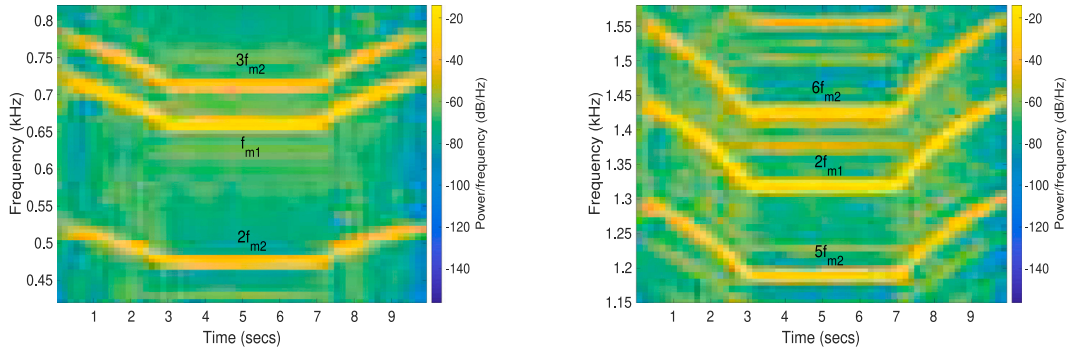


Fig. 22. Time-frequency representation of the acceleration signal under variable load.

3.2.4. Model simulation under varying load

Finally, to verify the model accuracy to consider non-stationary conditions, the varying load torque of Fig. 21(a) is used to simulate the system response and results are illustrated in Fig. 21(b–d). We can see that increasing the loading charge, causes a reduction in the operating speed and an increase of the amplitude of the phase currents and the vibration signal.

The time-frequency representation of the acceleration signal under this variable load is represented in Fig. 22. One can see the mesh frequencies variation in time. These results confirm the model ability to handle nonstationary conditions.

4. Conclusion

A theoretical and an experimental investigation of a motor-gearbox system composed of a three-phase induction machine and a parallel shaft two-stage gear system was proposed in this work to study the effect of local gear tooth defects on the systems' mechanical and electrical response. A lumped parameter model of the gearbox system was developed and enhanced by improving the process of calculation of the gear mesh stiffness, this was achieved by considering gears actual geometries and employing correlation measure to fit the simulation results with the experimental ones. The gearbox model was then coupled with a dynamical electrical model of the three phase motor in a way that allowed to consider transient effects during simulation. Vibrational and electrical simulated signals were analyzed and verified with measured signals for the validation of the proposed model under healthy and faulty conditions. The developed model showed a good efficiency to reproduce the system response at varying operating conditions. In addition, analysis of the vibrational and electrical signals allowed the detection of local gear tooth fault with a high degree of consistency. Finally, the model response was simulated for a varying input torque and results were analyzed in time and frequency domains.

As perspectives, the proposed model could be exploited in developing efficient indicators for the electromechanical machine health monitoring especially in nonstationary conditions. Also, the present study highlighted the lack of existing LPT-based models to consider gear mesh modulation by the gear rotation frequencies, this drawback could be a crucial driver for future researches.

Declaration of competing interest

The authors declare that they have no known competing financial interests or personal relationships that could have appeared to influence the work reported in this paper.

References

- [1] S.E. Lyshevski, *Electromechanical Systems and Devices*, CRC Press, 2008.
- [2] R. Parekh, AC Induction Motor Fundamentals, no. DS00887A, Microchip Technology Inc, 2003, pp. 1–24.
- [3] R. Merzouki, A.K. Samantaray, P.M. Pathak, B.O. Bouamama, *Intelligent Mechatronic Systems: Modeling, Control and Diagnosis*, Springer Science & Business Media, 2012.
- [4] S. Rezazadeh, J.W. Hurst, On the optimal selection of motors and transmissions for electromechanical and robotic systems, in: 2014 IEEE/RSJ International Conference on Intelligent Robots and Systems, IEEE, 2014, pp. 4605–4611.
- [5] R.E. Araújo, *Induction Motors: Modelling and Control*, BoD—Books on Demand, 2012.
- [6] N. Féki, G. Clerc, P. Velex, Gear and motor fault modeling and detection based on motor current analysis, *Electr. Power Syst. Res.* 95 (2013) 28–37.
- [7] Z. Zhou, Z. Chen, M. Spiryagin, E.B. Arango, P. Wolfs, C. Cole, W. Zhai, Dynamic response feature of electromechanical coupled drive subsystem in a locomotive excited by wheel flat, *Eng. Fail. Anal.* 122 (2021) 105248.
- [8] Q. Han, Z. Ding, X. Xu, T. Wang, F. Chu, Stator current model for detecting rolling bearing faults in induction motors using magnetic equivalent circuits, *Mech. Syst. Signal Process.* 131 (2019) 554–575.
- [9] Q. Han, T. Wang, Z. Ding, X. Xu, F. Chu, Magnetic equivalent modeling of stator currents for localized fault detection of planetary gearboxes coupled to electric motors, *IEEE Trans. Ind. Electron.* 68 (3) (2020) 2575–2586.
- [10] Z. Zhou, Z. Chen, M. Spiryagin, P. Wolfs, Q. Wu, W. Zhai, C. Cole, Dynamic performance of locomotive electric drive system under excitation from gear transmission and wheel-rail interaction, *Veh. Syst. Dyn.* (2021) 1–23, Publisher: Taylor & Francis, eprint: <https://doi.org/10.1080/00423114.2021.1876887>.
- [11] C. Kar, A. Mohanty, Monitoring gear vibrations through motor current signature analysis and wavelet transform, *Mech. Syst. Signal Process.* 20 (1) (2006) 158–187.
- [12] C. Kar, A. Mohanty, Vibration and current transient monitoring for gearbox fault detection using multiresolution Fourier transform, *J. Sound Vib.* 311 (1–2) (2008) 109–132.
- [13] S.H. Kia, H. Henao, G.-A. Capolino, Analytical and experimental study of gearbox mechanical effect on the induction machine stator current signature, *IEEE Trans. Ind. Appl.* 45 (4) (2009) 1405–1415.
- [14] S.H. Kia, H. Henao, G.-A. Capolino, Gear tooth surface damage fault detection using induction machine stator current space vector analysis, *IEEE Trans. Ind. Electron.* 62 (3) (2014) 1866–1878.
- [15] X. Chen, Z. Feng, Induction motor stator current analysis for planetary gearbox fault diagnosis under time-varying speed conditions, *Mech. Syst. Signal Process.* 140 (2020) 106691.
- [16] N. Feki, G. Clerc, P. Velex, An integrated electro-mechanical model of motor-gear units—Applications to tooth fault detection by electric measurements, *Mech. Syst. Signal Process.* 29 (2012) 377–390.
- [17] Y. Yi, D. Qin, C. Liu, Investigation of electromechanical coupling vibration characteristics of an electric drive multistage gear system, *Mech. Mach. Theory* 121 (2018) 446–459.
- [18] W. Bai, D. Qin, Y. Wang, T.C. Lim, Dynamic characteristic of electromechanical coupling effects in motor-gear system, *J. Sound Vib.* 423 (2018) 50–64.
- [19] J. Ottewill, A. Ruszczky, D. Broda, Monitoring tooth profile faults in epicyclic gearboxes using synchronously averaged motor currents: Mathematical modeling and experimental validation, *Mech. Syst. Signal Process.* 84 (2017) 78–99.
- [20] X. Liang, M.J. Zuo, Z. Feng, Dynamic modeling of gearbox faults: A review, *Mech. Syst. Signal Process.* 98 (2018) 852–876.
- [21] D. Yang, J. Lin, Hertzian damping, tooth friction and bending elasticity in gear impact dynamics, 1987.
- [22] Z. Chen, Z. Zhou, W. Zhai, K. Wang, Improved analytical calculation model of spur gear mesh excitations with tooth profile deviations, *Mech. Mach. Theory* 149 (2020) 103838.
- [23] H. Lin, J. Wang, F. Oswald, J. Coy, Effect of extended tooth contact on the modeling of spur gear transmissions, in: 29th Joint Propulsion Conference and Exhibit, 1993, p. 2148.
- [24] H. Ma, J. Zeng, R. Feng, X. Pang, B. Wen, An improved analytical method for mesh stiffness calculation of spur gears with tip relief, *Mech. Mach. Theory* 98 (2016) 64–80.
- [25] B. El Yousfi, A. Soualhi, K. Medjaher, F. Guillet, New approach for gear mesh stiffness evaluation of spur gears with surface defects, *Eng. Fail. Anal.* 116 (2020) 104740.
- [26] R. De Weerd, E. Tuinman, K. Hameyer, R. Belmans, Finite element analysis of steady state behavior of squirrel cage induction motors compared with measurements, *IEEE Trans. Magn.* 33 (2) (1997) 2093–2096.
- [27] M. Amrhein, P.T. Krein, 3-D magnetic equivalent circuit framework for modeling electromechanical devices, *IEEE Trans. Energy Convers.* 24 (2) (2009) 397–405.
- [28] A. Simion, L. Livadaru, A. Munteanu, Mathematical model of the three-phase induction machine for the study of steady-state and transient duty under balanced and unbalanced states, in: *Induction Motors: Modelling and Control*, 2012, p. 1.
- [29] H.H. Lin, C.-H. Liou, A Parametric Study of Spur Gear Dynamics, tech. rep., MEMPHIS UNIV TN, 1998.
- [30] B. El Yousfi, A. Soualhi, K. Medjaher, F. Guillet, A new analytical method for modeling the effect of assembly errors on a motor-gearbox system, *Energies* 14 (16) (2021) 4993.
- [31] P. Sainsot, P. Velex, O. Duverger, Contribution of gear body to tooth deflections—a new bidimensional analytical formula, *J. Mech. Des.* 126 (4) (2004) 748–752.
- [32] A.F. Del Rincon, F. Viadero, M. Iglesias, P. García, A. De-Juan, R. Sancibrian, A model for the study of meshing stiffness in spur gear transmissions, *Mech. Mach. Theory* 61 (2013) 30–58.
- [33] J. Zhan, M. Fard, R. Jazar, A CAD-FEM-QSA integration technique for determining the time-varying meshing stiffness of gear pairs, *Measurement* 100 (2017) 139–149.
- [34] J.E. Mottershead, M. Friswell, Model updating in structural dynamics: a survey, *J. Sound Vib.* 167 (2) (1993) 347–375.
- [35] S. Xue, R. Entwistle, I. Mazhar, I. Howard, The spur planetary gear torsional stiffness and its crack sensitivity under quasi-static conditions, 2016.
- [36] Y. Xiao, L. Fu, J. Luo, W. Shi, M. Kang, Nonlinear dynamic characteristic analysis of a coated gear transmission system, *Coatings* 10 (1) (2020) 39.